


## Efficient quantum process tomography for Clifford circuits

Shichuan Xue,<sup>\*</sup> Guangyao Huang,<sup>\*</sup> Yong Liu<sup>✉</sup>, Dongyang Wang, Weixu Shi,  
Yingwen Liu, Xiang Fu, Anqi Huang, Mingtang Deng, and Junjie Wu<sup>†</sup>

*Institute for Quantum Information & State Key Laboratory of High Performance Computing,  
College of Computer Science and Technology, National University of Defense Technology, Changsha 410073, China*

 (Received 26 June 2022; revised 4 January 2023; accepted 5 September 2023; published 20 September 2023)

A Clifford circuit is a pivotal tool in quantum computing and has extensive applications in quantum error correction codes and topological quantum computing. Hence, it is essential to benchmark and verify the effect of Clifford circuits against noise and errors. Standard quantum process tomography is a fundamental technique for fully characterizing quantum dynamics, but at the cost of exponential time, space, and computation with an increasing number of qubits. Here, we propose an efficient quantum process tomography method for Clifford circuits. Combining with the stabilizer formalism, we prove theoretically that, for an  $n$ -qubit Clifford circuit, our method merely needs  $m$  ancillary qubits and  $\lceil n/m \rceil$  input stabilizer states to obtain the quantum process. Numerical simulation results show that our method could perfectly rebuild the unknown Clifford quantum circuit with fidelity over 99.99% to six qubit cases. Our work provides an efficient and practical approach to benchmark and verify Clifford circuits.

DOI: [10.1103/PhysRevA.108.032419](https://doi.org/10.1103/PhysRevA.108.032419)

### I. INTRODUCTION

The Clifford circuit is a fundamental concept in quantum computing. Its elementary gates come from a Clifford group, which is generated by the Hadamard  $H$ , phase  $S$ , and controlled-NOT (CNOT) gates. Quantum circuits consist only of Clifford gates that can be efficiently simulated with a classical computer based on the Gottesman-Knill theorem [1,2]. Together with  $T$  gates, they can implement quantum computing [3].

Besides, the Clifford circuits have extensive applications in quantum error correcting (QEC) [4] and topological quantum computing (TQC). For instance, the typical phase flip code, bit flip code, and Shor code are all encoded by Clifford circuits; In the topological quantum computing scenario, the most promising non-Abelian anyon that can be realized in the laboratory is the Majorana zero mode (MZM) [5–14], which is capable of implementing topologically protected Clifford gates by braiding. Hence, it is important to put forward a benchmarking and verification tool for Clifford circuits.

Various benchmarking protocols have been proposed, including randomized benchmarking (RB) [15,16], direct fidelity estimation (DFE) [17], and so on. Nevertheless, these methods partially characterize a quantum system. Specifically, the RB method returns only an averaged sequence fidelity value, and the DFE method focuses on the fidelity value with the target. Therefore, quantum process tomography [1,18–20] still plays an indispensable role since it is a comprehensive characterization of quantum systems with full information. However, standard quantum process tomography (SQPT) [21,22] is not applicable to our problem. Exponential

costs of measurements, state preparation and storage, and computation are tremendous for practical and scalable usages.

Hence, in this paper, we put forward an efficient Clifford-circuit-oriented quantum process tomography method. Theoretically, we establish a correspondence between stabilizer formalism [1,23,24] and quantum process tomography. Specifically, for an  $n$ -qubit Clifford quantum process, we prove that our method needs only  $m$  ancillary qubits ( $m < n$ ) and prepares  $\lceil \frac{n}{m} \rceil$  stabilizer states as inputs to rebuild the quantum process. Compared with  $4^n$  input states and  $4^{2n}$  measurements in SQPT, our method is an efficient and practical tomography tool for the Clifford circuits. Numerically, we take randomly generated Clifford circuits as examples. Simulation results show a perfect reconstruction of the unknown Clifford quantum process up to six qubit cases with fidelity over 99.99%.

This paper is organized as follows: In Sec. II, we show the typical applications of the Clifford circuits in quantum computing. In Sec. III, we put forward the Clifford-circuit-oriented quantum process tomography method and give demonstrations through stabilizer formalism. We also present numerical simulations of our method on randomly generated Clifford circuits. We conclude in Sec. V.

### II. TYPICAL CLIFFORD CIRCUIT APPLICATIONS

Clifford circuits are widely used in quantum error correction and mitigation [25,26], topological quantum computation [27], and other topics. Here, we give two illustrative examples to show the versatile functionality of the Clifford circuits.

#### A. Quantum error correcting code circuit

Typical quantum error correction codes encode the target quantum states in a scheme tolerant to noise and error [1].

<sup>\*</sup>These authors contributed equally to this work.

<sup>†</sup>junjiewu@nudt.edu.cn

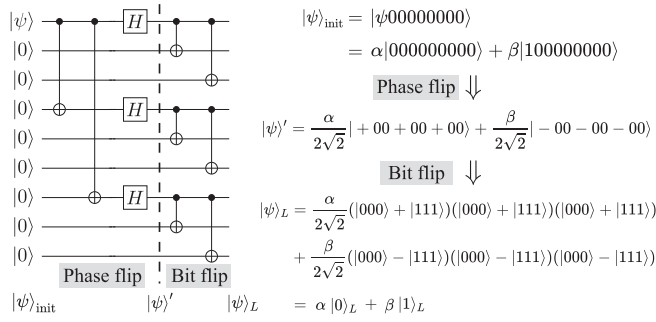


FIG. 1. Circuit diagram of the nine-qubit Shor code. It consists of a three-qubit phase encoding circuit and a three-qubit bit flip encoding circuit.

The information is then decoded to recover the state. Figure 1 gives an illustrative example of a Shor nine-qubit code encoding circuit [28], which contains a typical three-qubit phase flip (before the dashed line) and three-bit flip encoding circuits (after the dashed line). The Shor code utilizes another eight qubits  $|00, 000, 000\rangle_{2,\dots,9}$  for redundant encoding  $|\psi\rangle = \alpha|0\rangle + \beta|1\rangle$ . First, the phase flip circuit encodes the quantum state by  $|\psi\rangle|00, 000, 000\rangle \Rightarrow |\psi'\rangle$ , where  $|\pm\rangle = \frac{1}{\sqrt{2}}(|0\rangle \pm |1\rangle)$ . Second, the bit flip encoding circuits further transform the state to the logic quantum state  $|\psi\rangle_L$ . So finally, the nine-qubit code represents a logical qubit by  $|\psi\rangle_L = \alpha|0\rangle_L + \beta|1\rangle_L$ , where

$$\begin{aligned} |0\rangle_L &\equiv \frac{(|000\rangle + |111\rangle)(|000\rangle + |111\rangle)(|000\rangle + |111\rangle)}{2\sqrt{2}}, \\ |1\rangle_L &\equiv \frac{(|000\rangle - |111\rangle)(|000\rangle - |111\rangle)(|000\rangle - |111\rangle)}{2\sqrt{2}}. \end{aligned} \quad (1)$$

### B. Majorana zero mode based topological quantum computation

The next example of the Clifford circuit comes from a MZM-based topological quantum computation.

MZMs are quasiparticles exhibiting the non-Abelian statistics of the Ising anyon model, which is the most promising candidate of non-Abelian anyon for physical realization in solid-state systems. Compared with other non-Abelian anyons, one special property of MZMs in TQC is that the braiding of MZMs can only form a subset of Clifford gates. With the extra measurement feedback operation, all the Clifford gates can be implemented by braiding the MZMs. Here we summarize the concrete realization briefly.

Take a common choice of the logical qubit as an example. It is encoded by two pairs of MZMs,

$$|0\rangle_L = |00\rangle, \quad |1\rangle_L = |11\rangle. \quad (2)$$

In this logical encoding way, all the single-qubit Clifford gates can be realized by pure braiding of MZMs. Figures 2(a) and 2(b) show the generators of the single-qubit Clifford group, including the phase gate  $S$  and the Hadamard gate  $H$ .

However, the two-qubit entangled Clifford gates are forbidden by pure braiding. We added the measurement feedback operation to extend the ability of MZM-based TQC to the

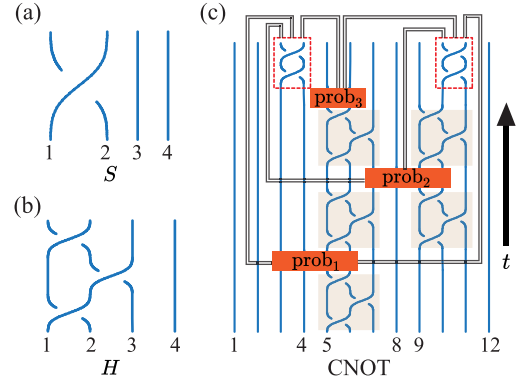


FIG. 2. Clifford gates in MZM-based TQC. (a) Phase gate  $S$ . (b) Hadamard gate  $H$ . (c) Measurement-based CNOT gate [15]. The control and target qubits are encoded in MZMs 1–4 and 9–12. The ancillary qubit is encoded in MZMs 5–8 and resets to  $|0\rangle$  for each action. The three parity measurements  $\text{prob}_{i=1,2,3}$  control the gates in the red dotted box.

whole Clifford gate. The CNOT gate we choose follows Ref. [29], which has the advantage of involving strictly local braiding operation. Figure 2(c) shows the measurement-based CNOT gate by braiding and measurements.

With these elementary gates  $S$ ,  $H$ , and CNOT in Fig. 2, all the Clifford gates can now be realized. Therefore, the MZM-based TQC is a perfect hardware foundation for our Clifford-circuit-oriented quantum process tomography theory.

We briefly review the mathematical details of MZM-based TQC in Appendix A, including the braid group representation, the remarks on different logical qubit encoding schemes, and the implication on the formations of the gates.

## III. CLIFFORD-CIRCUIT-ORIENTED QUANTUM PROCESS TOMOGRAPHY METHOD

### A. Quantum process tomography

Quantum process tomography is an essential technique in quantum information processing to characterize a quantum process [1].

However, standard quantum process tomography is a resource-demanding procedure, needing exponential time, space, and computation with the increasing number of qubits. Specifically, as shown in Fig. 3, it works by preparing an informationally complete set of input states  $|\psi_i\rangle$  and then

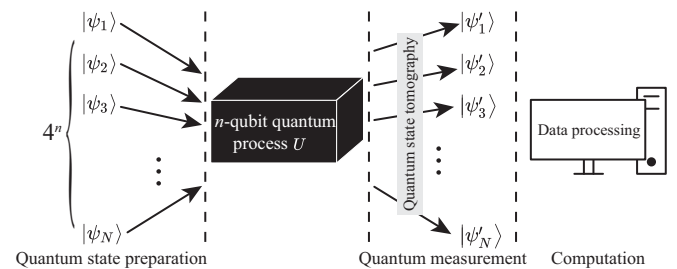


FIG. 3. The procedure of standard quantum process tomography with exponential cost on quantum state preparation, measurement, and computation.

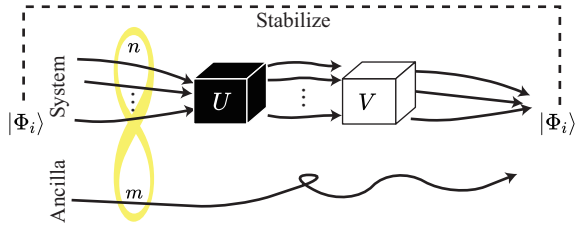


FIG. 4. The scheme of our Clifford-circuit-oriented quantum process tomography method.

performing the standard quantum state tomography on the corresponding output quantum states  $|\psi'_i\rangle$  [18,21,30]. As a result, the total number of quantum states needed to prepare is  $4^n$ , and the number of quantum measurements scales as  $4^{2n}$  for an  $n$ -qubit quantum process  $U$ . Besides, solving the inverse problem of state estimation involves huge computational costs [31,32]. Such exponential expenditures on state preparation, measurement, and computation severely limit the problem size on which SQPT can be feasibly applied. Currently, SQPT has only been experimentally implemented up to three qubits [20,33–37].

**B. Efficient Clifford-circuit-oriented quantum process tomography method**

In this section, we fully exploit the idea of the Hilbert-Schmidt test [38] (details in Appendix B) and put forward our efficient Clifford-circuit-oriented quantum process tomography method.

Specifically, for an  $n$ -qubit quantum process with  $m$  ancillaries ( $m \leq n$ ), our method follows these three steps, as shown in Fig. 4.

First, we merely need to prepare  $\lceil n/m \rceil$  ( $n + m$ )-qubit quantum states  $|\Phi_i\rangle$  as input to quantum process  $U$ . These quantum states entangle the system space and the ancillary space.

Second, we introduce a controllable quantum process  $V$  in system space to stabilize these input quantum states, i.e., adjusting  $V$  to satisfy  $VU \otimes I_{\text{anc}} |\Phi_i\rangle = |\Phi_i\rangle$ . We give the proof that when all these specific input states  $|\Phi_i\rangle$  are all stabilized, the overall quantum process  $VU \otimes I_{\text{anc}} = I_{\text{sys}} \otimes I_{\text{anc}}$ .

Finally, we deduce the unknown process  $U$  by  $V^{-1}$ .

It can be seen that our method shows considerable efficiency in state preparation (from  $4^n$  to practically  $\lceil n/m \rceil$ ) by introducing entanglement with arbitrary ancillary qubits. Our method can be rephrased and proved under the stabilizer formalism theory (see related theory in Appendix C). Next, in Secs. III C and III D, we utilize the theory of stabilizer formalism to analytically deduce the Clifford-circuit-oriented quantum process tomography protocol with full and fewer ancillary qubits, respectively. We analyze the number and the form of input states and show how these input states could stabilize the quantum process as an identity matrix.

**C. Clifford-circuit-oriented quantum process tomography with full ancillary qubits ( $m = n$ )**

When the ancillary qubits are full ( $m = n$ ), there needs only one maximally entangled quantum state as input, i.e.,

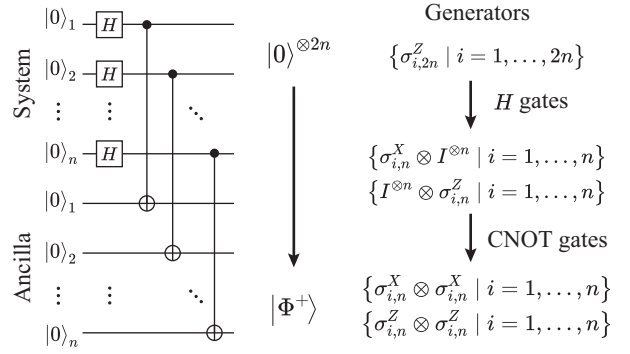


FIG. 5. The stabilizer circuit of  $|\Phi^+\rangle$  and its generators' evolution. The initial state and corresponding generators are known, and consequent evolution can be deduced via operator calculation with respect to the circuit gates.

$|\Phi^+\rangle = \frac{1}{\sqrt{d}} \sum_{j=1}^d |jj\rangle$ , where  $d = 2^n$ , as the Hilbert-Schmidt test circuit implies.

In the view of the stabilizer theory, the scheme of Clifford-circuit-oriented quantum process tomography is a stabilizer-solving problem. The input and output state  $|\Phi^+\rangle$  is a stabilizer state since the generating circuit contains Hadamard gates and CNOT gates only, as shown in Fig. 5. It can be stabilized by the overall quantum process  $\mathcal{E} \otimes I_{\text{anc}} = VU \otimes I_{\text{anc}}$  that  $\mathcal{E} \otimes I_{\text{anc}} |\Phi^+\rangle = |\Phi^+\rangle$ . Hence, in order to find the operator form of  $U$ , we need to utilize the stabilizer theory to analyze the generators of state  $|\Phi^+\rangle$ .

For such a stabilizer circuit, the Gottesman-Knill theorem [2,39] guarantees its efficient simulation, and we can directly deduce its generators and stabilizers via simple operators calculation, as listed beside the stabilizer circuit shown in Fig. 5. Finally, for this  $2n$ -qubit stabilizer state, there are  $2n$  generators in total. These  $2n$  generators are divided into two types. The first  $n$  generators are

$$\{\sigma_{i,n}^X \otimes \sigma_{i,n}^X \mid i = 1, \dots, n\}, \tag{3}$$

while the last  $n$  generators are

$$\{\sigma_{i,n}^Z \otimes \sigma_{i,n}^Z \mid i = 1, \dots, n\}, \tag{4}$$

where  $\sigma_{i,n}^{X(Y,Z)}$  denotes Pauli  $\sigma^X$ ,  $\sigma^Y$ , and  $\sigma^Z$  matrices at the  $i$ th qubit in an  $n$ -qubit identity operator string, for example,

$$\sigma_{i,n}^X = I \otimes I \otimes \dots \otimes \underbrace{\sigma_i^X}_{n} \otimes \dots \otimes I.$$

It can be seen that the corresponding generators in Eqs. (3) and (4) are always in a symmetric form—the first  $n$ -qubit operators are identical to the last  $n$ -qubit operators. Hence, the whole quantum process as a stabilizer has necessarily to be a symmetric form, thus limiting  $\mathcal{E} \otimes I_{\text{anc}}$  to the  $I_{\text{sys}} \otimes I_{\text{anc}}$  form. So one maximally entangled stabilizer state  $|\Phi^+\rangle$  as input is adequate to fix the intermediate stabilizer process as an identity matrix  $VU = I_{\text{sys}}$ , facilitating the consequent tomography procedure.

**D. Clifford-circuit-oriented quantum process tomography with fewer ancillary qubits ( $m < n$ )**

Clifford-circuit-oriented quantum process tomography with full ancillary qubits perfectly solves the exponential costs of state preparation, measurement, and computation in SQPT. However, it constrains the input state as a maximally entangled stabilizer state  $|\Phi^+\rangle$ , thus demanding the ancillary space as great as the system space. Hence, it still suffers from double the amount of qubits, which is quite an overhead and waste for quantum devices since the ancillary qubits undergo no operations in the protocol. Therefore, we propose a more general and efficient Clifford-circuit-oriented quantum process tomography method for arbitrary ancillary qubits. We prove that, for an  $n$ -qubit Clifford quantum process, our method needs only  $m$  ancillary qubits ( $m < n$ ) and prepares  $\lceil n/m \rceil$  entangled stabilizer states as inputs to rebuild the quantum process. Below we give theoretical explanations under the stabilizer formalism.

When the system qubits are  $n$ , and the ancillary qubits are  $m$  ( $m < n$ ), the stabilizer states could have many variations depending on the CNOT gates layout. We consider stabilizer circuits with  $n$  Hadamard gates and  $m$  CNOT gates. In the perfect condition with  $n$  ancillary qubits, the generators are symmetric between the first  $n$  qubits and the last  $n$  qubits. However, the symmetry is broken when reducing the ancillary qubits. It is essential to maintain the identity operator on the last  $m$ -qubit ancillary space in accordance with the  $VU \otimes I_{\text{anc}}$  form. However, regarding fewer ancillaries, we can have the following  $n + m$  generators in three types. There are  $m$  generators of the form

$$\{\sigma_{i,n}^X \otimes \sigma_{j,m}^X\}, \tag{5}$$

where indices  $i$  and  $j$  denote CNOT( $i, j$ ) gates with control qubit  $i$  and target qubit  $j$ . Likewise, the other  $m$  generators are

$$\{\sigma_{i,n}^Z \otimes \sigma_{j,m}^Z\}, \tag{6}$$

where

$$\sigma_{i,n}^Z = I \otimes I \otimes \dots \otimes \sigma_i^Z \otimes \dots \otimes I.$$

Moreover, the left  $r = n - m$  generators are

$$\{\sigma_{k,n}^X \otimes I^{\otimes m}\}, \tag{7}$$

where the index  $k$  denotes the system qubits without CNOT gates' control, therefore, it has no intersections with the  $m$  generators in Eq. (5).

Compared with the full ancillary condition in Eqs. (3) and (4), the symmetry is broken when reducing  $r$  ancillary qubits. There exist another  $r$  generators in Eq. (7), which are also possible stabilizer solutions with the form  $I_{\text{anc}}$ . Therefore, utilizing only one stabilizer state is not enough to distinguish the stabilizers between Eq. (7) and  $I_{\text{sys}} \otimes I_{\text{anc}}$ . So, it is necessary to add more input stabilizer states  $|\Phi_i\rangle$ . It is evident that, by introducing different CNOT gate configurations with control qubits covering all the system qubits, we can ensure that generators in Eq. (7) are distinguished from each other. Hence, the stabilizers could only be in the intersections of all the single state's stabilizer groups,

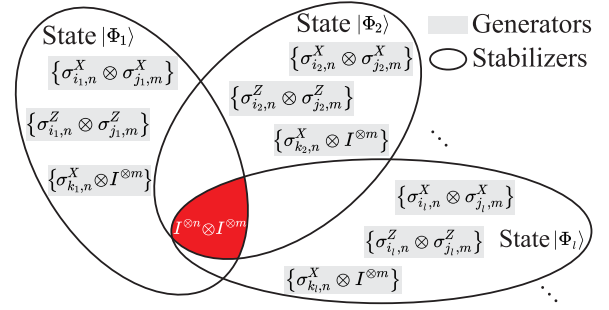


FIG. 6. Scheme of the Clifford-circuit-oriented quantum process tomography with fewer ancillary qubits. Venn graph of different stabilizer states' stabilizer groups. All the stabilizers form a group in the elliptical, and the rectangular shaded box denotes the corresponding generators. The red shaded area denotes the intersection stabilizers of different input states, limited at  $I^{\otimes n} \otimes I^{\otimes m}$ , that can stabilize all the stabilizer states simultaneously.

fixed at  $I_{\text{sys}} \otimes I_{\text{anc}}$ , as shown in the red shaded area in Fig. 6. Specifically, for an  $n$ -qubit Clifford quantum process with  $m$  ancillary qubits ( $m < n$ ), we need to prepare  $\lceil n/m \rceil$  entangled stabilizer states as input. Figure 7 shows the organization of the stabilizer circuits. We split the system qubits  $\{q_1^s, q_2^s, \dots, q_n^s\}$  into  $\lceil n/m \rceil$  disjoint subsets (different shaded parts), for example,  $\{q_1^s, q_2^s, \dots, q_m^s\}$ ,  $\{q_{m+1}^s, q_{m+2}^s, \dots, q_{2m}^s\}$ ,  $\dots, \{q_{\lceil n/m \rceil - 1}^{s} m + 1, \dots, q_n^s\}$ . In each stabilizer circuit, one of these subsets is the set of controlling qubits of CNOT gates, and the ancillary qubits,  $\{q_{n+1}^a, q_{n+2}^a, \dots, q_{n+m}^a\}$ , is the set of the target qubits of CNOT gates (arrows in the figure).

Here, to better understand the scheme of our method with  $m$  ancillary qubits, we give an instance of a two-qubit Clifford circuit with one ancillary qubit. As proved in the paper,  $\lceil 2/1 \rceil = 2$  stabilizer states are inputs, and the CNOT gates

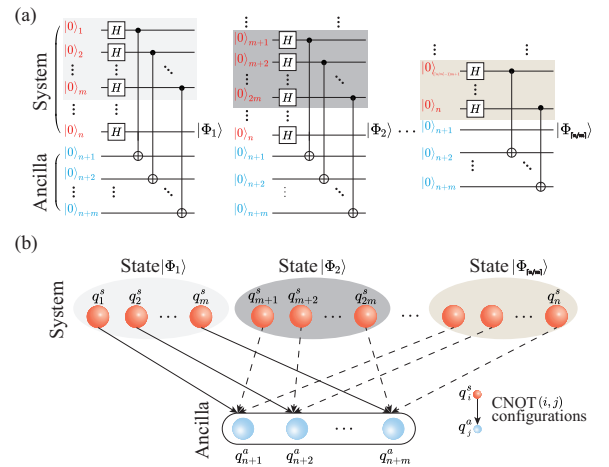


FIG. 7. Illustration of the stabilizer circuits with fewer ancillaries. (a) The stabilizer circuit layouts. These  $\lceil n/m \rceil$  stabilizer circuits go through a layer of  $n$  Hadamard gates in the system space and different CNOT( $i, j$ ) gate configurations. These stabilizer circuits correspond to stabilizer states  $|\Phi_i\rangle$ . (b) Different CNOT( $i, j$ ) gate configurations. We group the system qubits into  $\lceil n/m \rceil$  parts (different shaded groups). In each stabilizer circuit, the CNOT gates cover the selected system qubits and the ancillary qubits (arrows in figure).

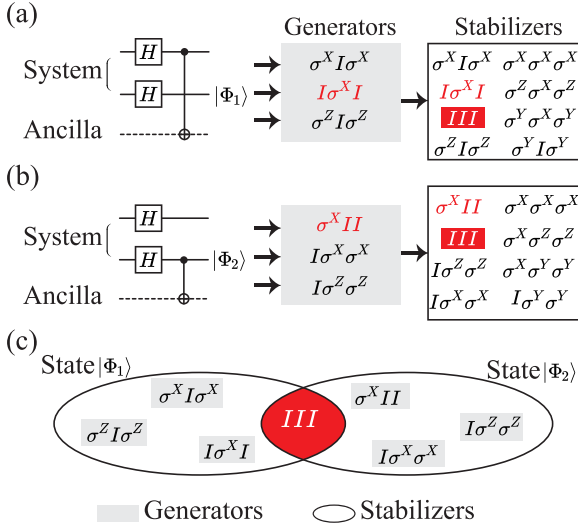


FIG. 8. An example of two-qubit Clifford circuit quantum process tomography with one ancillary qubit. Panels (a) and (b) show two input stabilizer circuits with two system qubits and one ancillary qubit, related to two stabilizer states  $|\Phi_1\rangle$  and  $|\Phi_2\rangle$ , respectively. Corresponding generators and stabilizers are also listed. (c) Venn graph of the two stabilizer groups. By introducing one more stabilizer state, the two stabilizer groups can fix the intersection stabilizer at  $III$ .

layout should distinguish from each other to cover all the  $n$  target qubits. So we choose the following two stabilizer states  $|\Phi_1\rangle = (|000\rangle + |010\rangle + |101\rangle + |111\rangle)/2$  and  $|\Phi_2\rangle = (|000\rangle + |011\rangle + |100\rangle + |111\rangle)/2$  as shown in Figs. 8(a) and 8(b), where the CNOT gates vary in the control qubit. The final translated generators and stabilizers are listed beside. It is clear that using only one stabilizer state could not guarantee that the quantum process is an identity matrix since there are generators of the form  $\{I\sigma^X I, \sigma^X II\}$  (red characters). Therefore, it is impossible to distinguish them from  $III$ . By introducing the second stabilizer state, the common generator can only be  $III$ , as shown in the red shaded operator in Fig. 8(c). Hence, it is feasible to conduct the consequent stabilizer solving.

To conclude, it needs  $\lceil n/m \rceil$  stabilizer states as inputs to constrain the stabilizer form, where the  $\lceil n/m \rceil$  input stabilizer states consist of different CNOT gates configurations covering all the  $n$  system qubits.

#### IV. NUMERICAL SIMULATION

The Clifford-circuit-oriented quantum process tomography method can be utilized as a benchmarking and verification tool. In this section, we conduct numerical simulations to validate our process tomography protocol.

##### A. Simulation framework

We utilize the numerical simulation framework in Fig. 9(a) to conduct typical tasks. The simulation mainly involves input stabilizer states preparation, target Clifford quantum process  $U$ , parametric quantum circuit (PQC)  $V(\vec{\theta})$ , and classical processing unit. We take the randomly generated Clifford circuit

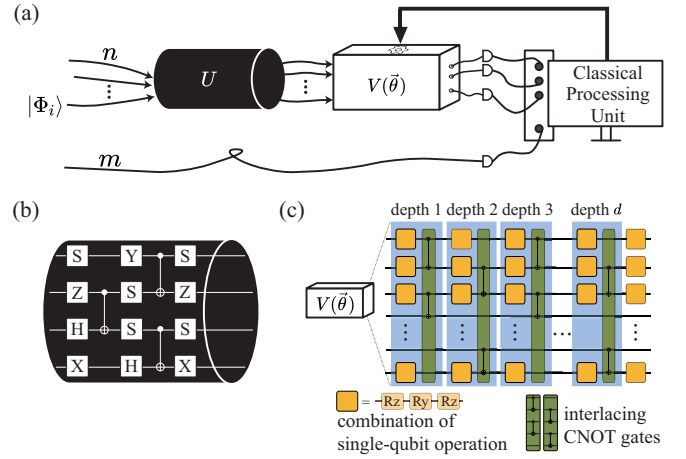


FIG. 9. Numerical simulation structure of the Clifford-circuit-oriented quantum process tomography. (a) The scheme consists of the Clifford-circuit-oriented quantum process tomography and the classical processing unit. The quantum process tomography part mainly involves the preparation of faithful input stabilizer states  $|\Phi_i\rangle$ , the evolution of the target quantum process (black channel  $U$ ), and the controllable PQC [white boxed  $V(\vec{\theta})$ ]. The classical processing unit is composed of the output state evaluation and classical optimizing and updating. (b) A typical four-qubit randomly generated Clifford circuit. (c) The ansatz structure of the PQC  $V(\vec{\theta})$ .

as the unknown quantum process to show the feasibility of our protocol.

Figure 9(b) gives an illustrative example. The randomly generated Clifford circuit is organized layer by layer. The single-qubit gate is randomly picked from the single-qubit Clifford gate group (total 24 gates), and the two-qubit CNOT gates are interlaced depending on the circuit depth.

Following the unknown quantum process  $U$ , we utilize a PQC  $V(\vec{\theta})$  to rebuild the Clifford process. Here, we use the most general circuit ansatz—hardware-efficient ansatz [40] as the PQC structure [shown in Fig. 9(c)]. It is organized depth by depth. For each circuit depth, there is a single-qubit gate layer (yellow gates) composed of three rotational gates. The sequence  $R_z$ ,  $R_y$ , and  $R_z$  ensure that arbitrary single qubit rotations can be produced with appropriate parameters,

$$R_y(\theta) = \begin{bmatrix} \cos \frac{\theta}{2} & -\sin \frac{\theta}{2} \\ \sin \frac{\theta}{2} & \cos \frac{\theta}{2} \end{bmatrix}, \quad R_z(\theta) = \begin{bmatrix} e^{-i\frac{\theta}{2}} & 0 \\ 0 & e^{i\frac{\theta}{2}} \end{bmatrix}. \quad (8)$$

In addition, there is another two-qubit gate layer to entangle all the qubits (green layer). The CNOT gates are arranged by different depths—for odd depth, the CNOT gates are  $\text{CNOT}(i, i + 1)$ , ( $i = 1, 3, 5, \dots$ ) and for even depth the CNOT gates are  $\text{CNOT}(i, i + 1)$ , ( $i = 2, 4, 6, \dots$ ) [41].

In the classical processing part, we define the loss function as the infidelity between the input states and the output states:

$$f(\vec{\theta}) = \sum_i [1 - F(|\Phi_i\rangle, V(\vec{\theta})U \otimes I|\Phi_i\rangle)], \quad (9)$$

where  $F$  denotes the state fidelity measure. Then, based on a gradient-based optimization algorithm [42], we continuously update the parameters in the  $V(\vec{\theta})$  circuit. Meanwhile, we add parameter approximation at certain epochs to maintain the

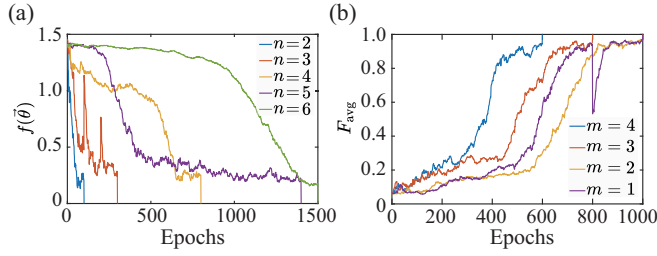


FIG. 10. Numerical simulation results of the randomly generated Clifford quantum process tomography. (a) The relation between the loss function  $f(\vec{\theta})$  and the iteration epochs. Different colored lines correspond to different numbers of qubits. Here,  $n = m$  and  $n = 2, 3, 4, 5, 6$ . (b) The relation between the average quantum gate fidelity  $F_{\text{avg}}$  and the iteration epochs on four-qubit randomly generated Clifford quantum process tomography. Here,  $n = 4$ ,  $m \leq n$ , and different colored lines correspond to different ancillaries  $m$ .

Clifford discrete feature since the optimization procedure is continuous.

### B. Results analysis

As proved in Sec. III, when the loss function  $f(\vec{\theta})$  goes down to zero, the overall quantum process is approaching  $V(\vec{\theta})U \otimes I = I \otimes I$ . Here, we evaluate the experimental results using the average quantum gate fidelity [43]. The average gate fidelity  $F_{\text{avg}}$  between the rebuilt  $\mathcal{U}$  and the real  $\mathcal{E}$  is given by

$$F_{\text{avg}}(\mathcal{U}, \mathcal{E}) = \int d\psi \langle \psi | \mathcal{U}^\dagger \mathcal{E}(|\psi\rangle\langle\psi|) \mathcal{U} | \psi \rangle, \quad (10)$$

where the integral is taken according to the uniform Haar-invariant probability measure on state vectors  $|\psi\rangle$ . Actually, the average quantum gate fidelity  $F_{\text{avg}}(\mathcal{U}, \mathcal{E})$  has a relationship with the diamond norm  $\|\mathcal{U} - \mathcal{E}\|_\diamond$ , which is generally used to compare different quantum channels [44]. For simplicity, we utilize the average quantum gate fidelity  $F_{\text{avg}}$  to characterize the numerical simulation results.

Numerically, we first conducted simulations from two-qubit cases to six-qubit cases ( $n = 2, 3, \dots, 6$ ) with full ancillaries  $m = n$ . Figure 10(a) shows our method is scalable and feasible for accurate reconstruction of the Clifford quantum process. The unknown Clifford quantum process is perfectly rebuilt by the parametric quantum circuit with loss function  $f(\vec{\theta})$  close to zero and fidelity over  $F_{\text{avg}} \geq 99.99\%$ . Further in Fig. 10(b), we simulated a four-qubit Clifford circuit quantum process with ancillary qubits  $m \leq 4$ . It is validated that our protocol is available under fewer ancillary qubits cases.

### C. Robustness discussion

In this section, we discuss how physical noise influences our Clifford-circuit-oriented process tomography method.

First, we consider the noise existence during the variational optimization. Since the Clifford circuit quantum process tomography is run on the quantum system, there are unavoidable noise and error when evaluating the loss function  $f(\vec{\theta})$  and calculating the gradient. Here, we suppose the unknown

TABLE I. Numerical simulation results of noise  $\epsilon \sim N(0, \sigma)$  during variational optimization among 200 trials.

$\epsilon \sim N(0, \sigma)$	0	0.01	0.02	0.03	0.04
Max. $F_{\text{avg}}$	99.99%	99.99%	99.82%	99.32%	98.86%
Avg. $F_{\text{avg}}$	79.60%	78.99%	78.82%	73.77%	78.30%

process is still a perfect Clifford circuit, while the protocol running procedure might introduce noise. In the numerical simulations, we utilize the typical Gaussian noise  $\epsilon \sim N(0, \sigma)$  to simulate the noisy optimization environment. Specifically, we directly added the noise  $\epsilon$  onto the output state  $V(\vec{\theta})U \otimes I|\Phi_i\rangle$  in the loss function (9). We set the noise level as  $\sigma = 0.01, 0.02, 0.03, 0.04$ . For each noise configuration, we repeat the simulation 200 times, and the results are illustrated in Table I. It can be seen that our Clifford-circuit-oriented tomography method has considerable robustness against noise during the optimization procedure. Second, we consider the target Clifford circuit is not perfect and may be only ‘‘close to the Clifford’’ process. Under such assumptions, our protocol is actually not applicable from a theoretical aspect since the theory proof is based on the stabilizer formalism with the *a priori* information that the unknown process is a stabilizer process. Here, we analyze the robustness of our protocol on the deviation of the target quantum process.

For the randomly generated Clifford circuit, the single-qubit gate is randomly picked from the single-qubit Clifford gate group (total 24 gates), which is the combination of a phase  $S$  gate and a Hadamard gate  $H$ . We assume that there exist deviations in these two elementary gates so that the practical gates are

$$S'(\epsilon) = \begin{bmatrix} e^{i(-\frac{\pi}{4} + \epsilon)} & 0 \\ 0 & e^{i(\frac{\pi}{4} + \epsilon)} \end{bmatrix},$$

$$H'(\epsilon) = \begin{bmatrix} \cos(\frac{\pi}{4} + \epsilon) & \sin(\frac{\pi}{4} + \epsilon) \\ \sin(\frac{\pi}{4} + \epsilon) & -\cos(\frac{\pi}{4} + \epsilon) \end{bmatrix}, \quad (11)$$

where  $\epsilon$  is also sampled from a Gaussian distribution  $\epsilon \sim N(0, \sigma)$ . Hence, the resulting Clifford circuit is a noisy process. Similarly, we conduct 200 repetitive trials for each noisy configuration, and the results are listed in Table II.

For nonperfect Clifford circuits, our approach shows stable performance against gate noise. Since the parameter optimization is a continuous procedure, it has a fault-tolerance feature during the optimization. Therefore, from the above twofold

TABLE II. Numerical simulation results of noise on single-qubit elementary gates.

$\epsilon \sim N(0, \sigma)$	0.00	0.01	0.02	0.03	0.04
Max. $F_{\text{avg}}$	99.99%	99.99%	99.99%	99.99%	99.99%
Avg. $F_{\text{avg}}$	79.60%	80.12%	75.60%	69.41%	73.51%
$\epsilon \sim N(0, \sigma)$	0.05	0.06	0.07	0.08	0.09
Max. $F_{\text{avg}}$	99.99%	99.99%	99.99%	99.93%	99.91%
Avg. $F_{\text{avg}}$	70.69%	71.74%	68.87%	64.99%	71.08%

analysis, we can conclude that our protocol is robust against noise.

## V. CONCLUSION

In our previous work [45], we put forward a general tomography method for arbitrary  $n$ -qubit unitary quantum processes. With arbitrary  $m$  ancillary qubits, the input states needed are  $2^{n-m}$ . In this work, utilizing similar entanglement assistance, we found a more efficient conclusion for Clifford circuits. We combined the theory of stabilizer formalism and quantum process tomography and proposed a more efficient tomography method. Theoretically, we prove that, for an  $n$ -qubit Clifford circuit, our approach merely needs  $m$  ancillary qubits and  $\lceil n/m \rceil$  input stabilizer states to rebuild the quantum process, utilizing the stabilizer formalism. It shows considerable advantages in state preparation (from  $4^n$  to practically  $\lceil n/m \rceil$ ) by introducing entanglement with arbitrary ancillary qubits. Numerically, we conduct simulations of our method on randomly generated Clifford circuits up to six-qubit cases. Results show an accurate reconstruction of the unknown Clifford quantum process with fidelity over 99.99%. Our work shows a further application of the method in Ref. [45] and provides a more efficient and practical approach to Clifford-circuit-oriented quantum process tomography.

## ACKNOWLEDGMENTS

We thank Chu Guo for the fruitful discussion. We appreciate the helpful discussion with other members of the QUANTA group, including Siqi Wang, Yang Wang, Pingyu Zhu, Yuzhen Zheng, Qilin Zheng, and Hao Cheng. J.W. acknowledges support from the National Natural Science Foundation of China under Grants No. 62061136011, No. 62075243, and No. 62105366.

## APPENDIX A: MAJORANA ZERO MODE BASED TOPOLOGICAL QUANTUM COMPUTATION

In this Appendix, we give a brief review of the MZM-based topological quantum computation. Detailed reviews can be found in Refs. [46–49].

Since the MZMs belong to the Ising anyon model, we first discuss the computational power of the MZM from this model. The Ising anyon model is a set of particles with different topological charge  $\{1, \psi, \sigma\}$ , where 1 is the vacuum,  $\psi$  is the fermion, and  $\sigma$  denotes the MZM. These particles obey the fusion rules:

$$\psi \times \psi = 1, \quad \psi \times \sigma = \sigma, \quad \sigma \times \sigma = 1 + \psi. \quad (\text{A1})$$

The last fusion rule of  $\sigma$  particle (MZM) indicates its non-Abelian anyonic nature, and the braiding of MZM performs the TQC.

The exchange of non-Abelian anyons is depicted by braid group  $\mathcal{B}_n$ , where  $n$  is the number of MZMs. A general braid operation  $B_l$  can be decomposed as the product of the group generators  $b_i$

$$B_l = \prod_{i=1, \dots, n-1, \text{ and } j \in \mathbb{Z}} b_i^j. \quad (\text{A2})$$

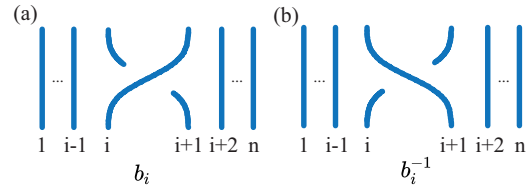


FIG. 11. The braiding scheme of the Majorana operators  $b_i$  and its inverse.

The corresponding Majorana operator  $\gamma$  of the MZM can be deduced from the spinor representation of the braid group [50]

$$\{\gamma_i, \gamma_j\} = 2\delta_{i,j}, \quad \gamma_i^\dagger = \gamma_i. \quad (\text{A3})$$

In terms of Majorana operators  $\{\gamma_i\}$ , the braid group generator  $b_i$  can be written as

$$b_i = e^{-\frac{\pi}{4}\gamma_i\gamma_{i+1}} = \frac{e^{i\frac{\pi}{4}}}{\sqrt{2}}(1 - \gamma_i\gamma_{i+1}). \quad (\text{A4})$$

Figure 11 shows the action of  $b_i$ .

A pair of MZMs can represent a single qubit via the observable parity  $-i\gamma_1\gamma_2|\psi_\pm\rangle = \pm|\psi_\pm\rangle$ . It becomes evident if we define the fermionic operators for each pair of MZMs,

$$f_j = \frac{1}{2}(\gamma_{2j-1} + i\gamma_{2j}), \quad (\text{A5})$$

then the qubit states are vacuum  $|0\rangle$  and  $|1\rangle = f_1^\dagger|0\rangle$ , which is equivalent because  $|0\rangle \rightarrow |\psi_-\rangle$ ,  $|1\rangle \rightarrow |\psi_+\rangle$ . However, this is not true. There is a superselection rule stating that any local operators cannot change the total topological charge. Considering a pair of MZMs, their fusion can be a vacuum (as  $|0\rangle$ ) or a fermion (as  $|1\rangle$ ), and they possess different topological charges. Thus the qubit cannot be in a superposition state  $\alpha|0\rangle + \beta|1\rangle$ , because the particles with different topological charges cannot convert to each other.

Therefore, to represent  $n$  logical qubits, the minimal number of MZMs should be  $2n + 2$  (that is,  $n + 1$  pairs). Unfortunately, in the Hilbert space of this compact encoding, certain single-qubit and two-qubit Clifford gates are missing by pure braiding for  $n \geq 3$  [51].

Another choice of encoding of the logical qubits is that one logical qubit is encoded by two pairs of MZMs with a total topological charge of 1 (vacuum),

$$|0\rangle_L = |00\rangle, \quad |1\rangle_L = |11\rangle = f_1^\dagger f_2^\dagger |00\rangle, \quad (\text{A6})$$

where the subscript  $L$  labels the logical qubit. This choice of encoding spans a subspace of the whole MZM Hilbert space. One advantage of this encoding is that all the single-qubit Clifford gates can be realized through pure braiding.

The representation of the gate is related to the braid group element  $B_l$  as

$$[B_l]_{ij} = {}_L\langle i|B_l|j\rangle_L = \langle ii| \prod_{k,h} b_k^h |jj\rangle. \quad (\text{A7})$$

For example,  $b_2^2 = \sigma^X$  is the Pauli  $\sigma^X$  gate,  $b_1 b_2 b_1$  is the Hadamard gate (an irrelevant global phase has been neglected). Figure 2 shows the single-qubit Clifford gates by braiding.

As mentioned in the main text, a measurement-based CNOT gate with parity measurements [29] is adopted as an example

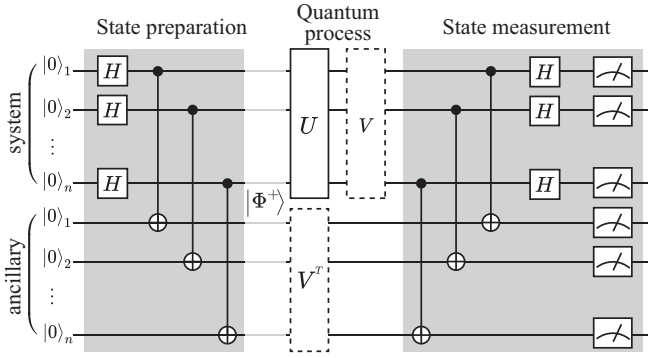


FIG. 12. Hilbert-Schmidt test circuit. It consists of state preparation, quantum processes, and state measurement.

for the two-qubit entangled gate. We note that there are other proposals [52–55] of measurement-based CNOT gate by MZMs, and each has its advantages. The concrete realization of the CNOT gate will not affect the analysis of our method.

### APPENDIX B: HILBERT-SCHMIDT TEST

To begin with, we borrow the idea of the Hilbert-Schmidt test [38], as illustrated in Fig. 12. The Hilbert-Schmidt test circuit was initially utilized as a tool to give the Hilbert-Schmidt inner product of two  $n$ -qubit operators  $U$  and  $V$ . It is realized through an extended Hilbert space consisting of entangled state preparation, quantum operations, and measurements. First, it needs another  $n$  ancillary qubits to extend the original Hilbert space, preparing the input state as a maximally entangled state between the system and ancillary qubits, i.e.,  $|\Phi^+\rangle = \frac{1}{\sqrt{d}} \sum_{j=1}^d |jj\rangle$ , where  $d = 2^n$ . Second, the overall entangled system evolves under the operator,  $\mathcal{E} \otimes I_{\text{anc}} = VU \otimes I_{\text{anc}}$ . Finally, we conduct a state measurement on the bell basis in the end, and the output probability is the absolute value of the inner product between  $U$  and  $V$  as shown in Eq. (B1):

$$|\langle \Phi^+ | (VU) \otimes I_{\text{anc}} | \Phi^+ \rangle|^2 = \frac{1}{d^2} |\text{Tr}(VU)|^2. \quad (\text{B1})$$

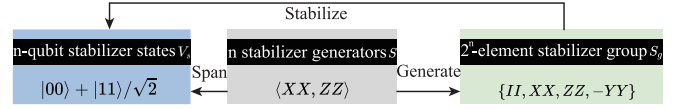


FIG. 13. Relationship between stabilizer states, stabilizer group, and stabilizer generators.

It can be seen that, when the output state  $(VU) \otimes I_{\text{anc}} |\Phi^+\rangle$  remains identical to the input  $|\Phi^+\rangle$ , we can arrive at  $\text{Tr}(VU) = d$ , hence  $VU = I_{\text{sys}}$ . Therefore, we can utilize a controllable  $V$  to rebuild the unknown  $U = V^{-1}$ . Specifically, when the number of ancillary qubits is  $n$ , it is viable to transpose the controllable  $V$  parameters from the system space to the ancillary space. It is supported by the quantum ricochet property  $I \otimes X |\Phi^+\rangle = X^T \otimes I |\Phi^+\rangle$ , as shown in the dashed box in Fig. 12. Therefore, the circuit depth could be further shortened.

### APPENDIX C: THE STABILIZER FORMALISM INTRODUCTION

Stabilizer formalism is a powerful tool for understanding a comprehensive class of operations in quantum computation. There are mainly three key elements involved in our method: stabilizer states, stabilizers, and generators.

Stabilizer states are generated by stabilizer circuits with P, Hadamard, and CNOT gates only. The feature is that all the basis amplitude is equal. For an  $n$ -qubit stabilizer state, we could always find  $2^n$  stabilizers to stabilize it. Mathematically,  $S_i |\psi\rangle = |\psi\rangle$ .

Interestingly, the stabilizers  $S_i$  form an Abelian group satisfying

$$S := \{S_i\} \text{ s.t. } -I \notin S \text{ and } \forall S_i, S_j \in S, [S_i, S_j] = 0. \quad (\text{C1})$$

The stabilizer generator is the maximum independent subset  $S_g$  of the stabilizer group  $S$ . It means that any element of the stabilizer group can be generated as a product of the stabilizer generators. There is an obvious conclusion illustrated in Fig. 13 that the  $n$ -qubit stabilizer states can be uniquely determined by a stabilizer group of size  $2^n$ , which is generated by  $n$  generators. Hence, it is clear that stabilizer formalism can efficiently characterize quantum states and operators.

[1] N. Chuang, *Quantum Computation and Quantum Information* (Cambridge University Press, Cambridge, 2000).  
 [2] D. Gottesman, [arXiv:quant-ph/9807006](https://arxiv.org/abs/quant-ph/9807006).  
 [3] S. Bravyi and A. Kitaev, *Phys. Rev. A* **71**, 022316 (2005).  
 [4] S. J. Devitt, W. J. Munro, and K. Nemoto, *Rep. Prog. Phys.* **76**, 076001 (2013).  
 [5] A. Y. Kitaev, *Phys. Usp.* **44**, 131 (2001).  
 [6] F. Wilczek, *Nat. Phys.* **5**, 614 (2009).  
 [7] M. Leijnse and K. Flensberg, *Semicond. Sci. Technol.* **27**, 124003 (2012).  
 [8] J. Alicea, *Rep. Prog. Phys.* **75**, 076501 (2012).  
 [9] M. Franz, *Nat. Nanotechnol.* **8**, 149 (2013).  
 [10] C. Beenakker, *Annu. Rev. Condens. Matter Phys.* **4**, 113 (2013).

[11] S. R. Elliott and M. Franz, *Rev. Mod. Phys.* **87**, 137 (2015).  
 [12] R. Aguado, *Riv. Nuovo Cimento* **40**, 523 (2017).  
 [13] R. M. Lutchyn, E. P. Bakkers, L. P. Kouwenhoven, P. Krogstrup, C. M. Marcus, and Y. Oreg, *Nat. Rev. Mater.* **3**, 52 (2018).  
 [14] J.-B. Fu, B. Li, X.-F. Zhang, G.-Z. Yu, G.-Y. Huang, and M.-T. Deng, *Sci. China: Phys., Mech. Astron.* **64**, 107001 (2021).  
 [15] E. Knill, D. Leibfried, R. Reichle, J. Britton, R. B. Blakestad, J. D. Jost, C. Langer, R. Ozeri, S. Seidelin, and D. J. Wineland, *Phys. Rev. A* **77**, 012307 (2008).  
 [16] E. Magesan, J. M. Gambetta, and J. Emerson, *Phys. Rev. Lett.* **106**, 180504 (2011).  
 [17] S. T. Flammia and Y.-K. Liu, *Phys. Rev. Lett.* **106**, 230501 (2011).



- [18] G. M. D'Ariano and P. LoPresti, *Phys. Rev. Lett.* **86**, 4195 (2001).
- [19] M. Mohseni, A. T. Rezakhani, and D. A. Lidar, *Phys. Rev. A* **77**, 032322 (2008).
- [20] J. L. O'Brien, G. J. Pryde, A. Gilchrist, D. F. V. James, N. K. Langford, T. C. Ralph, and A. G. White, *Phys. Rev. Lett.* **93**, 080502 (2004).
- [21] I. L. Chuang and M. A. Nielsen, *J. Mod. Opt.* **44**, 2455 (1997).
- [22] J. F. Poyatos, J. I. Cirac, and P. Zoller, *Phys. Rev. Lett.* **78**, 390 (1997).
- [23] S. Aaronson and D. Gottesman, *Phys. Rev. A* **70**, 052328 (2004).
- [24] K. Fujii and K. Fujii, *Quantum Computation with Topological Codes: From Qubit to Topological Fault-Tolerance* (Springer, Singapore, 2015).
- [25] M. Gutiérrez, L. Svec, A. Vargo, and K. R. Brown, *Phys. Rev. A* **87**, 030302(R) (2013).
- [26] P. Czarnik, A. Arrasmith, P. J. Coles, and L. Cincio, *Quantum* **5**, 592 (2021).
- [27] S. Bravyi and D. Gosset, *Phys. Rev. Lett.* **116**, 250501 (2016).
- [28] P. W. Shor, *Phys. Rev. A* **52**, R2493 (1995).
- [29] O. Zilberberg, B. Braunecker, and D. Loss, *Phys. Rev. A* **77**, 012327 (2008).
- [30] S. Aaronson, *Proc. R. Soc. London, Ser. A* **463**, 3089 (2007).
- [31] K. Banaszek, G. M. D'Ariano, M. G. A. Paris, and M. F. Sacchi, *Phys. Rev. A* **61**, 010304(R) (1999).
- [32] C. Ferrie, *Phys. Rev. Lett.* **113**, 190404 (2014).
- [33] R. C. Bialczak, M. Ansmann, M. Hofheinz, E. Lucero, M. Neeley, A. D. O'Connell, D. Sank, H. Wang, J. Wenner, and M. Steffen, *Nat. Phys.* **6**, 409 (2010).
- [34] A. M. Childs, I. L. Chuang, and D. W. Leung, *Phys. Rev. A* **64**, 012314 (2001).
- [35] A. Shabani, R. L. Kosut, M. Mohseni, H. Rabitz, M. A. Broome, M. P. Almeida, A. Fedrizzi, and A. G. White, *Phys. Rev. Lett.* **106**, 100401 (2011).
- [36] M. Riebe, K. Kim, P. Schindler, T. Monz, P. O. Schmidt, T. K. Körber, W. Hänsel, H. Häffner, C. F. Roos, and R. Blatt, *Phys. Rev. Lett.* **97**, 220407 (2006).
- [37] L. Govia, G. Ribeill, D. Ristè, M. Ware, and H. Krovi, *Nat. Commun.* **11**, 1084 (2020).
- [38] S. Khatri, R. LaRose, A. Poremba, L. Cincio, A. T. Sornborger, and P. J. Coles, *Quantum* **3**, 140 (2019).
- [39] D. Gottesman, *Stabilizer Codes and Quantum Error Correction* (California Institute of Technology, California, 1997).
- [40] A. Kandala, A. Mezzacapo, K. Temme, M. Takita, M. Brink, J. M. Chow, and J. M. Gambetta, *Nature (London)* **549**, 242 (2017).
- [41] S. Xue, Y. Liu, Y. Wang, P. Zhu, C. Guo, and J. Wu, *Phys. Rev. A* **105**, 032427 (2022).
- [42] J. C. Spall *et al.*, *IEEE Trans. Autom. Control* **37**, 332 (1992).
- [43] M. A. Nielsen, *Phys. Lett. A* **303**, 249 (2002).
- [44] M. Kliesch and I. Roth, *PRX Quantum* **2**, 010201 (2021).
- [45] S. Xue, Y. Wang, J. Zhan, Y. Wang, R. Zeng, J. Ding, W. Shi, Y. Liu, Y. Liu, A. Huang *et al.*, *Phys. Rev. Lett.* **129**, 133601 (2022).
- [46] A. Y. Kitaev, *Ann. Phys. (NY)* **303**, 2 (2003).
- [47] P. Bonderson, K. Shtengel, and J. Slingerland, *Ann. Phys. (NY)* **323**, 2709 (2008).
- [48] C. Nayak, S. H. Simon, A. Stern, M. Freedman, and S. DasSarma, *Rev. Mod. Phys.* **80**, 1083 (2008).
- [49] J. K. Pachos, *Introduction to Topological Quantum Computation* (Cambridge University Press, Cambridge, 2012).
- [50] C. Nayak and F. Wilczek, *Nucl. Phys. B* **479**, 529 (1996).
- [51] A. Ahlbrecht, L. S. Georgiev, and R. F. Werner, *Phys. Rev. A* **79**, 032311 (2009).
- [52] S. B. Bravyi and A. Y. Kitaev, *Ann. Phys. (NY)* **298**, 210 (2002).
- [53] S. Bravyi, *Phys. Rev. A* **73**, 042313 (2006).
- [54] T. Hyart, B. vanHeck, I. C. Fulga, M. Burrello, A. R. Akhmerov, and C. W. J. Beenakker, *Phys. Rev. B* **88**, 035121 (2013).
- [55] G. M. D'Ariano and P. LoPresti, *Phys. Rev. Lett.* **91**, 047902 (2003)..